ANNALS OF GEOPHYSICS, 69, 6, 2026; doi:10.4401/ag-9564
OPEN ACCESS

# Enhancing Resolution in Local Passive Seismic Tomography: Adaptive Grid Implementation at Agung Volcano, Indonesia

I Putu Raditya Ambara Putra[*,1], David Prambudi Sahara[2], Wahyu Hidayat[1], Sri Widiyantoro[2], Andri Dian Nugraha[2]

(1) Geophysical Engineering, Faculty of Technology Mineral and Energy, UPN Veteran Yogyakarta, Yogyakarta 55283, Indonesia
(2) Global Geophysics Research Group, Faculty of Mining and Petroleum Engineering, Institut Teknologi Bandung, Bandung 40132, Indonesia

Article history: received April 1, 2026; accepted October 29, 2026

## Abstract

Passive seismic tomography is a widely used method for imaging subsurface structures, relying on natural seismicity sources without the need for artificial sources. Grid-node parameterisation is a key aspect of subsurface reconstruction in passive seismic tomography. Although many data distribution-based adaptive grid-node methodologies and schemes have been developed, their implementation in local-scale passive seismic tomography is still very limited. In particular, no adaptive grid scheme has yet been applied to Agung Volcano, despite the 2017 eruption involving a notably complex magma migration phase. In response to this, we implemented an adaptive grid scheme in passive seismic tomography to investigate the local structure of Agung Volcano using data from the 2017 eruption and compared the results with those obtained using a fixed grid scheme. In the computing process, we use the Python programming language, considering its well-established and popular ecosystem. We conducted synthetic tests to examine the validity of our calculation process, and the results indicate that the calculations and inversion scheme are accurate and robust to be implemented for real data. The results of real data inversion show that the adaptive grid scheme produces significantly lower RMS residual values compared to the conventional fixed grid scheme. In addition, there is a clear increase in spatial resolution compared to the initial grid configuration, which facilitates more accurate interpretation of subsurface structures and more precise delineation of magmatic system boundaries.

Keywords: Passive Seismic tomography; Adaptive grid; Subsurface imaging; Agung Volcano; resolution

## 1. Introduction

Passive seismic tomography has become a commonly used method in imaging subsurface structures. This method provides an overview of how wave velocity is distributed beneath the surface. This method can be applied across a wide range of spatial scales, from global and regional investigations to the local characterization of specific sites. Its significance is further underscored by a broad functional spectrum, encompassing applications such as the

identification and delineation of subduction zone structures (Chiarabba and Amato, 2003; Dobretsov et al., 2015; Eberhart-Phillips and Michael, 1998; Neri et al., 2009; Replumaz et al., 2010; Thurber et al., 1995). This method has also been successfully applied to the mapping of volcanic magmatic systems, exploration and monitoring of geothermal sources (Amoroso et al., 2018; Bai and Greenhalgh, 2005; Battaglia et al., 2008; Foix et al., 2021; Garcia et al., 2019; Heath et al., 2015; Jousset et al., 2015; Koulakov, 2022; Lees, 2007; Nugraha et al., 2019). Moreover, this method has also been applied at the local scale for monitoring underground mining activities (Hidayat et al., 2024; Luxbacher et al., 2008; Mercier et al., 2015; Qian et al., 2018; Westman et al., 2012; Yang et al., 2025, 2026).

The basis of the tomography inversion process lies in the parameterisation of the grid/nodal model as a representation of the subsurface space (Vesnaver, 1996). Historically, regular grids have dominated practical implementations due to computational simplification, although mathematically there is no restriction to use a specific grid shape (Sambridge and Rawlinson, 2005). However, this approach has fundamental limitations, which is its inability to accurately represent complex geological features due to the rigidity of the grid shape. Another problem in passive seismic tomography is that we are unable to flexibly control the distribution of ray paths. This is because the distribution of events and stations in passive seismics is uneven. As a result, there will be disparities in the number of rays passing through grid nodes, with some nodes being passed by many rays and others by few (Böhm et al., 2000; Fang et al., 2022).

The simplest strategy for addressing ray path density disparities between grid nodes is through a seismic data selection process based on ray path similarity, as practised by previous studies (Nolet, 2023; Widiyantoro and Hilst, 1997). However, this approach is less effective in the context of local tomography, which faces data limitations. The next method used to accommodate data distribution is to adjust the density of grid nodes with a dense grid in the target area and a sparse grid in the surrounding area (Eberhart-Phillips, 1990; Thurber, 1987), as well as a grid construction method based on a priori data (Abers and Roecker, 1991; Curtis and Snieder, 1997). Although both approaches conceptually accommodate the characteristics of data distribution, their implementation is not dynamically integrated into the inversion process itself. An emerging alternative solution is the adaptation of grid-node geometry that dynamically adapts to the spatial distribution pattern of the data. This adaptation methodology includes null-energy-based optimisation (Böhm et al., 2000; Kamath et al., 2015; Spakman and Bijwaard, 2001; Vesnaver, 1996), nodal adaptation based on spatial seismic velocity gradients (Böhm et al., 2000; Sambridge and Faletič, 2003), and irregular grid-node configurations based on raypath distribution within the gridnode (Zhang and Thurber, 2005).

Grid-node parametrisation in seismic tomography is a crucial factor, not only in terms of its dimensions and shape, but also its orientation and position. One approach to reducing the influence of such parameterisation was developed by Michelini (1995), whereby the inversion is carried out simultaneously for both the velocity parameters and the positions of the grid points on the discretisation mesh. This allows the grid-node positions to adjust during the inversion process, thereby making the model parameterisation more flexible. Another approach was then developed and introduced as the Weighted Average Model (WAM), in which the tomography process is run simultaneously in multiple orientations, and the results are subsequently averaged (Calo et al., 2013, 2009). It is expected that this will minimise the effects of grid position and orientation. This methodology was subsequently implemented in the latest version of the LOTOS software (Koulakov, 2009).

Despite various data-driven adaptive passive seismic tomography methodologies that have been developed, their practical implementation in local-scale studies remains relatively infrequent. Most local tomography implementations still rely on rigid and constant grid nodes. In our view, this is due to the simplification of calculations and limited availability of open-source code that provides the automatic adaptive grid features. One example is tomography imaging of Agung Volcano (Ardianto et al., 2021). Agung Volcano has unique and interesting characteristics to study, particularly during the 2017 eruption period when the distribution of volcano-tectonic earthquakes was not concentrated directly beneath the summit but shifted towards the northwest. Based on previous studies (Ardianto et al., 2021; Syahbana et al., 2019), the 2017 eruption of Mount Agung can be divided into three main phases. The first phase was characterised by the ascent of magma from a depth of around 14 km, which lasted from March to September 2017. The second phase was characterised by a dyke intrusion extending towards the area between Agung Volcano and Mount Abang, marked by a significant increase in seismic activity from late September to October 2017. The presence of this intrusion was also successfully modelled using Interferometric Synthetic Aperture Radar (InSAR) data in a previous study (Albino et al., 2019). The third phase was marked by the migration of magma towards a shallow reservoir, which occurred from early to mid-November 2017. This phase was characterised by a change in earthquake type, from volcano-tectonic (VT) earthquakes to low-frequency earthquakes and tremors, indicating fluid movement at shallow depths.

The description of these three phases of the eruption indicates the complexity of the magma migration process during the 2017 Agung Volcano eruption. The tomography study using a fixed grid scheme successfully mapped the distribution of general anomalies and their relationship with the magma migration phase, but the results tended to be oversmooth, making it difficult to represent the position and dimensions of the anomaly area in greater detail and precision. Based on these observations, there is a necessity to apply methodologies that enhance the spatial resolution and accuracy of tomographic imaging results of Agung Volcano.

In this study, we introduce the implementation of an adaptive grid scheme in the tomography of Agung Volcano. The primary objective is to evaluate the extent to which adaptive gridding improves imaging results compared to conventional fixed-grid approaches, particularly in the context of passive seismic tomography applied to volcanic settings. We adopted an approach that had been used previously, by enabling the grid to adjust according to ray path density (Zhang and Thurber, 2005). The adaptive scheme is expected to provide clearer and sharper velocity contrasts and boundaries, resulting in more realistic and detailed subsurface representations as demonstrated in previous studies (Scarfì et al., 2007). All computational procedures were developed in Python, chosen for its flexibility and robust scientific ecosystem. The anticipated outcome of this approach is an improved delineation of anomaly positions and geometries, offering a more accurate depiction of subsurface structures than that achieved through traditional fixed grid tomography.

## 2. Data and Method

In this study, we utilized volcano-tectonic earthquake data from Agung Volcano's 2017 eruption (8 seismic stations; 2,726 events). This dataset facilitated both real data tomographic inversion and the generation of synthetic data for synthetic validation tests. The hypocenter location was determined in three steps. The first step is to use

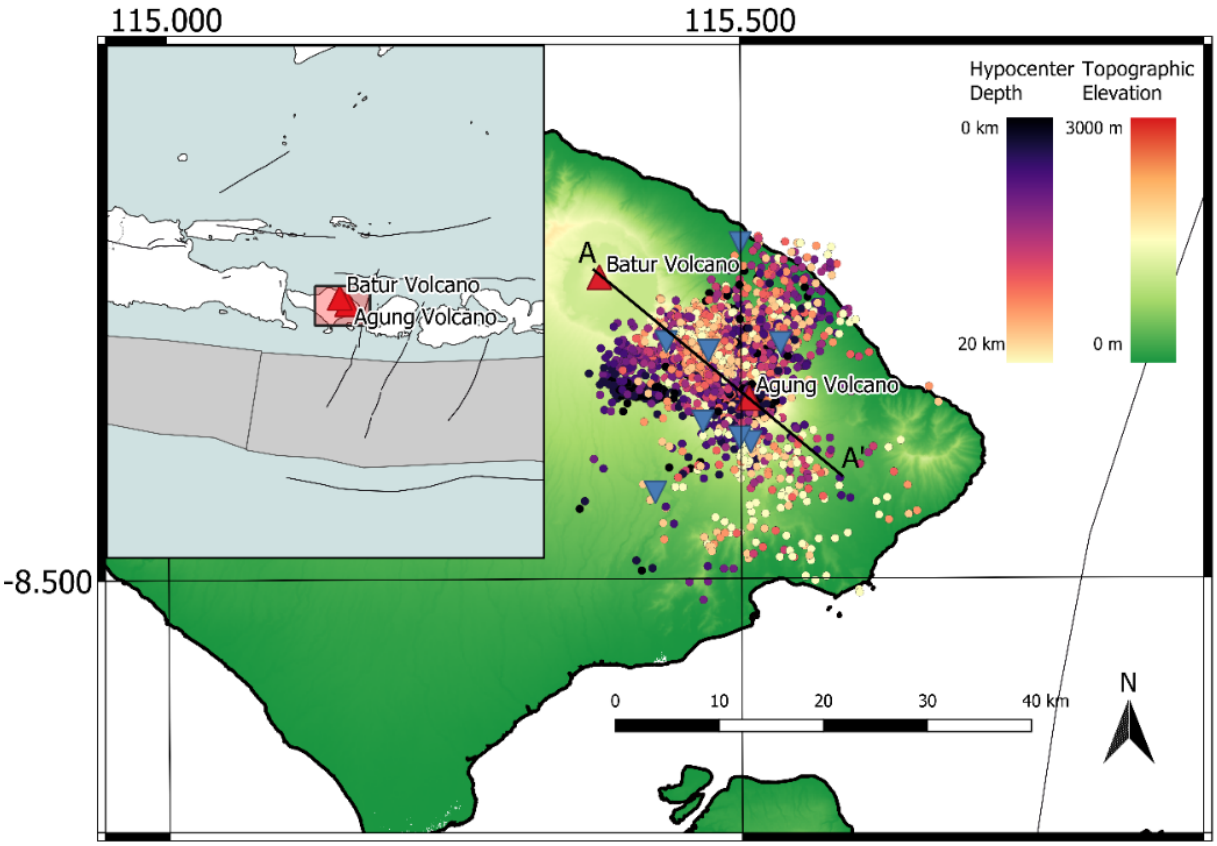



**Figure 1.** Location of Agung and Batur Volcano in Bali, Indonesia. The position of the hypocenter data (Sahara et al., 2021) used in this study, where color denotes depth, is shown by the colored dots. The black lines labeled A-A′ indicate the locations of the cross sections shown in this study. An inverted blue triangle indicates the position of the recording station.

the NonLinLoc program to identify the location (Lomax et al., 2000). The velocity model used in this step was the Kou09 1-D seismic velocity model (Koulakov et al., 2009). The next step involves utilizing Velest software to update the 1D model and station correction (Kissling et al., 1995, 1994). The velocity model for this step is known as Agu20. The last step was relocation using the Double – Difference method in the HypoDD program (Waldhauser, 2000). Details regarding the processing of waveform data to obtain the hypocenter catalog have been described by (Sahara et al., 2021). Figure 1 illustrates the spatial distribution of earthquake occurrences in the Agung Volcano region of Bali, as well as the positioning of seismometer stations utilized in this study.

## 2.1 Mathematical Equation

According to the ray theory, the arrival time from an earthquake source i to a station k $T_k^i$, is expressed as,

$$T_k^i = \tau^i + \int_i^k u ds \tag{1}$$

where $\tau^i$ is origin time of event i, $u$ is slowness, and $ds$ is partition of the ray path. The relationship between arrival time, source location, origin time, and velocity structure (Eq. 1) is not linear, therefore it is linearized and can be written as,

$$r_k^i = \sum_{l=1}^{3} \frac{\partial T_k^i}{\partial x_l^i} \Delta x_l^i + \Delta\tau^i + \int_i^k \delta u \, ds \tag{2}$$

$\frac{\partial T_k^i}{\partial x_l^i}$ is the perturbation of the hypocenter parameter of event i, $\Delta\tau^i$ is the perturbation of the origin time of event i, and $\delta u$ is the slowness perturbation. The details of Eq. (2) can be found in C. H. Thurber (1983). If Eq. (2) is made in the form of a matrix for 1 event i which has a total arrival time of Ni, then the form will be obtained.

$$\boldsymbol{A}_i \Delta xi + \boldsymbol{B}_i \Delta m = \Delta T_i \tag{3}$$

$\boldsymbol{A}_i$ (Ni × 4) is a matrix of partial derivative of the event hypocenter, and $\boldsymbol{B}_i$ (Ni × L) is a matrix partial derivative of the slowness model (length of the raypath partition traversed at each grid node). $\Delta xi$ is the perturbation vector from the hypocenter location and origin time, $\Delta m$ is the slowness model perturbation vector, and $\Delta T_i$ is the residual travel time vector. The form of Eq. (3) when combined for all earthquake events will become a linear equation,

$$\boldsymbol{GY} = \Delta \boldsymbol{T} \tag{4}$$

If the total number of arrival time data is Nt and the number of events is P, $\boldsymbol{G} = [\boldsymbol{AB}]$ or can be called a kernel matrix measuring (Nt × 4P + L), $\boldsymbol{Y} = \begin{bmatrix} \Delta x \\ \Delta m \end{bmatrix}$ has dimensions of $4P + L$. We then apply norm damping and smooth damping, so Eq. (4) will be,

$$\begin{bmatrix} \boldsymbol{G} \\ \mu 1 \boldsymbol{I} \\ \mu 2 \boldsymbol{D} \end{bmatrix} \boldsymbol{Y} = \begin{bmatrix} \Delta \boldsymbol{T} \\ 0 \\ 0 \end{bmatrix} \tag{5}$$

where ($\mu 1$, $\mu 2$) is a scaling constant, $\boldsymbol{I}$ is an identity matrix, and D is a non-square matrix, as applied by (Sambridge and Faletič, 2003).

Finally, add the diagonal scaling matrix S, and the equation becomes,

$$\begin{bmatrix} \boldsymbol{G} \\ \mu 1 \boldsymbol{I} \\ \mu 2 \boldsymbol{D} \end{bmatrix} \boldsymbol{S}\boldsymbol{Y}' = \begin{bmatrix} \Delta \boldsymbol{T} \\ 0 \\ 0 \end{bmatrix} \tag{6}$$

Matrix $\boldsymbol{S}$ is a diagonal weighting matrix whose value is inversely proportional to the root volume of the grid node, while $\boldsymbol{Y}' = \boldsymbol{S}^{-1}\boldsymbol{Y}$. The application of this weighting aims to prevent the ray partition length at large grid node volumes from dominating the inversion process.

## 2.2 Ray Tracing

We applied the pseudo-bending approach of Um and Thurber (1987) to perform ray tracing. This method is a two-point method, which begins by guessing the initial path between two points, and then pertubates iteratively until the travel time decreases and reaches a convergence point. This approach has the advantage of being capable of accurately predicting the travel time and path of waves in 3D heterogeneous environments, even though it is only an approximation and does not solve the ray equation directly. Another advantage is that it is quite efficient in terms of computational time.

To validate the accuracy of the ray-tracing code that we compiled, we compared the results of our calculations with those obtained from the TomoDD program (Zhang, 2003). We conducted the test using data from Agung Volcano collected at the eight previously mentioned stations. We evaluated the performance of our calculation using two different velocity models: a 1D vertical layer model and a 1D vertical layer model with an added low-velocity block beneath the Agung Volcano. The difference average in the first model was $6.81 \times 10^{-4}$ s with a standard deviation $8.53 \times 10^{-4}$ s, while the difference average in the second model was $4.60 \times 10^{-3}$ with a standard deviation of $7.21 \times 10^{-3}$ s. Although the basic principle of ray tracing that we use is the same as tomoDD, our scheme differs fundamentally in path initialisation. TomoDD searches for curvatures that produce the lowest travel time, while we use simple straight lines as initialisation. There are also differences in terms of numerical precision. This is proven by constant model tests that are simple to calculate the analytical results. Validation on the constant model shows that the average difference between our algorithm and the analytical results ($6.45 \times 10^{-14}$ s) is 12 orders of magnitude smaller than tomoDD ($7.77 \times 10^{-5}$ s), with a lower standard deviation ($1.21 \times 10^{-13}$ s and $7.17 \times 10^{-5}$ s).

These findings underscore the robustness and reliability of the ray-tracing calculations employed in the inversion process. While some deviations from tomoDD are observed, their magnitudes remain relatively minor and are substantially smaller than the discrepancies between the pseudobending method and the analytical solution reported by Um and Thurber (1987), which ranged from 0.0006 to 0.3 s depending on the complexity of the model. This result highlights that the approach adopted in this study yields more consistent and dependable accuracy within the context of seismic modelling.

## 2.3 Adaptive Node – Tomographic Inversion Scenario

Our developed algorithm employs a Voronoi-based grid constructed from irregular nodal geometry. This approach provides significant flexibility in defining grid dimensions and positioning during the inversion process. For conventional regular-grid inversions, users may simply input uniformly spaced nodal coordinates. Additionally, we adopted the methodological approach employed by Zhang and Thurber (2005), which incorporates functionality for dynamically adding or removing nodes during the inversion procedure. We used a Ray Hit Count (RHC), which is the number of rays that travel through a single Voronoi grid, as the threshold for adding and eliminating nodes.

First, a regular node is set up. Then, we perform ray tracing for all the data and calculate the total ray that passes through each node. Then, we created a Tetrahedron grid from the existing nodes. Each tetrahedron had four constituent nodes. If the sum of RHC from the four constituent nodes is higher than threshold1, a new node will be added in the middle of the tetrahedron (Fig. 2). Nodes with an RHC below threshold2 will be deleted. The next step was to compile the kernel matrix according to Eq. (6). We implemented the method described by Sambridge

and Faletič (2003) to calculate the length of the raypath partition passing through irregular nodes. This involves dividing the raypath into smaller sections for more accurate measurement. After the kernel matrix based on Eq. (6) is formed, the next step is to find the solution to the linear equation system using the LSQR method (Paige and Saunders, 1982a, 1982b; Saunders, 1995) available in the scipy or numpy package. The LSQR method was chosen because it is very effective when applied to large-scale sparse matrix cases. Following this process, the model is updated, and the subsequent step involves executing velocity interpolation on an intermediate regular computational grid. An intermediate grid was created to facilitate ray-tracing calculations using the devised pseudo-bending method.

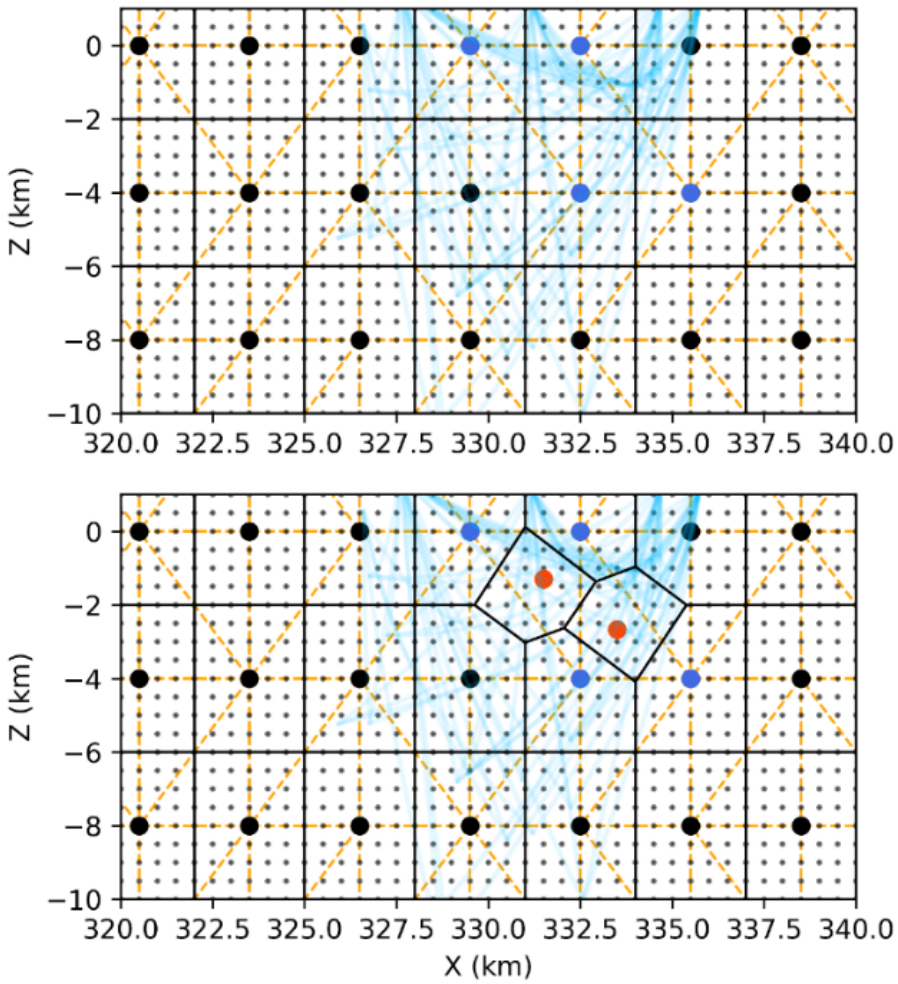



**Figure 2.** Illustration of the grid adaptation scheme and Voronoi grid constructed based on node positions (only an illustrative example, not the actual data processing). The black dots represent the initial input nodes. The blue dots represent the 4 nodes forming 2 tetrahedrons. The red dots are nodes added at the centre of the tetrahedron with RHC values above the set threshold. The lower graph shows the final Voronoi grid after nodes are added. The blue lines represent raypath illustrations. The smaller, densely packed black dots are the intermediate regular grid used in the ray tracing process.

To ensure proper functioning of the intermediate grid, it is essential that the spacing between its respective grid is less than that of the primary grid. If the RMS after the model is updated is smaller than the defined threshold, the process is completed, otherwise, the above process is repeated until the RMS is smaller than the defined threshold. The flowchart of the adaptive node-tomographic inversion process is shown in Fig. 3. This process involves the simultaneous inversion of both Vp and Vs in a single matrix. From the equation derived in the mathematical equation section above, hypocenter parameters (location and origin time) were also updated alongside the velocity model.

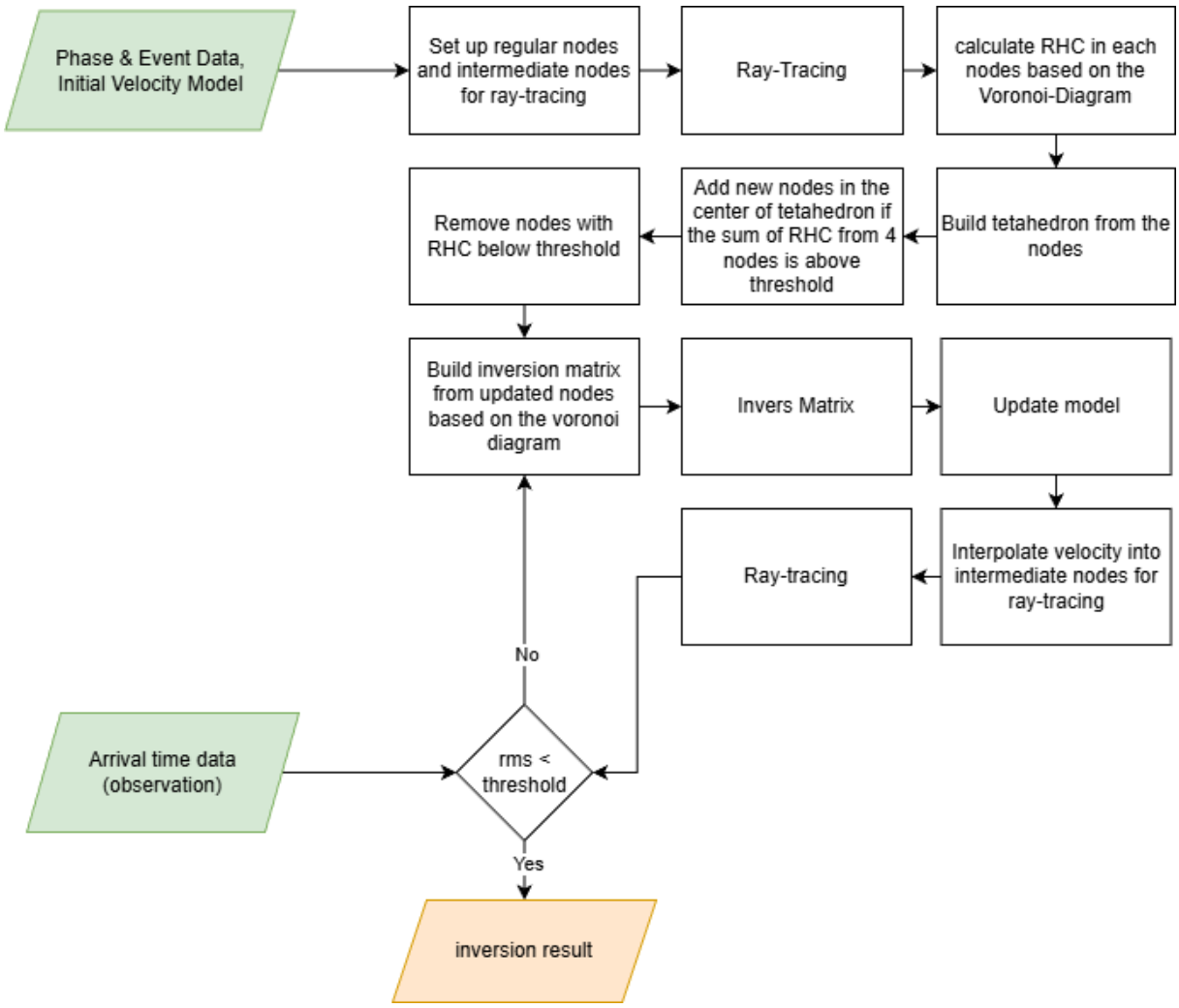



**Figure 3.** Flowchart of inversion process.

# 3. Results and Discussion

## 3.1 Synthetic Data Inversions

To evaluate the performance, sensitivity and robustness of the inversion methods used, four synthetic tests were carried out with models of varying complexity. The four models were designed to test the ability of the fixed-grid and adaptive-grid schemes to reconstruct velocity structures under anomaly geometry conditions that differed from the initial grid parameterisation. Furthermore, for each synthetic model, normally distributed random noise was added at noise levels of 1% and 3% to evaluate the sensitivity of the inversion results to disturbances in the synthetic travel time data.

The first synthetic model is the standard checkerboard (CKB) model. In this model, positive and negative velocity anomalies are arranged according to the initial grid-node positions on the grid-node used in the inversion process, with a size of $3 \times 3 \times 4$ km. Consequently, the boundaries of the anomalies align with the boundaries of the initial grid-node parameterisation. This model is used as a baseline test to evaluate the ability of the inversion method to reconstruct anomaly patterns when the geometry of the synthetic model matches the inversion grid-node parameterisation.

The second synthetic model was designed by modifying the positions of the anomalies from the standard CKB model. The size and basic pattern of the anomalies remained at $3 \times 3 \times 4$ km, but all of the anomaly positions were shifted relative to the node positions on the starting grid-node used in the inversion. This modification aims to increase the complexity of the test by creating a mismatch between the actual positions of the anomalies and the

initial grid parameterisation. Consequently, this test is specifically used to evaluate the sensitivity of both schemes to changes in the positions of the anomalies and to determine whether the adaptive grid is capable of providing a better representation when the actual structure no longer follows the boundaries of the initial grid-node.

The third synthetic model is a low-velocity block model that is relatively simple compared to the CKB model. To increase the model's complexity, the boundary of the low-velocity anomaly was then shifted so that it no longer align with the boundary of the initial grid-nodes used in the inversion process. In addition, positive velocity anomalies were introduced at depths of less than 4 km and greater than 10 km, as shown in Fig. 6.

The fourth synthetic model is the most complex velocity model and was created based on the results of the inversion of observational data using an adaptive scheme. This model represents a more heterogeneous velocity structure and exhibits more complex spatial variations than the previous three models. Furthermore, the grid-node distribution in this model is irregular as a consequence of the adaptive parameterisation process. The model was then used as the true model to generate synthetic travel time data, which was subsequently inverted again using both fixed-grid and adaptive-grid schemes. This test aimed to evaluate the ability of both methods to reconstruct complex velocity structures that more closely approximate actual subsurface conditions.

The results of the synthetic tests for the first, second, third and fourth models are shown in Figs. 4, 5, 6 and 7 respectively. The results presented here compare the adaptive grid and fixed grid schemes using synthetic data with a noise level of 3%. Meanwhile, the results of the tests with a noise level of 1% are presented in the Supplementary Materials.

To evaluate the performance comparison between the adaptive grid and fixed grid schemes, a series of quantitative tests were carried out based on three key metrics. Firstly, data misfit was measured using the Root Mean Square Error (RMS) residual value at the final iteration after the inversion process had converged. Secondly, model recovery was analysed by comparing the absolute values of P-wave and S-wave velocities (Vp and Vs) between the synthetic model and the inversion results, including the RMS residual, Mean Absolute Error (MAE) and correlation coefficient. Thirdly, anomaly recovery is evaluated by comparing the perturbation values (dVp and dVs) relative to the 1-D reference model, using similar statistical metrics, which is RMS residual, MAE and correlation. Given the differences in grid-node geometry between the two schemes, all of these statistical analyses were applied to the velocity values interpolated onto the intermediate grid used during the inversion process to ensure spatial consistency. The results of the quantitative metrics are shown in Table 1.

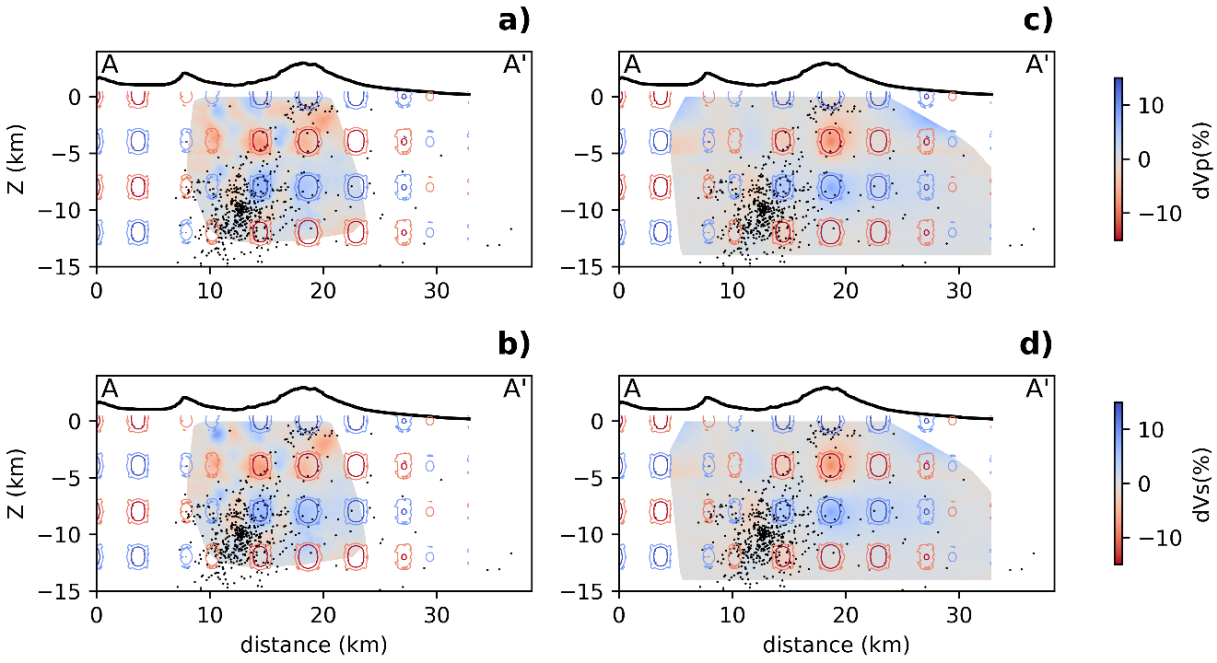



**Figure 4.** Results of the CKB synthetic test for the adaptive grid scheme (a and b) and the fixed grid scheme (c and d), for the parameters dVp (a and c) and dVs (b and d) respectively. The contour lines in each figure represent the synthetic checkerboard model used as a reference, with red indicating negative anomalies and blue indicating positive anomalies.

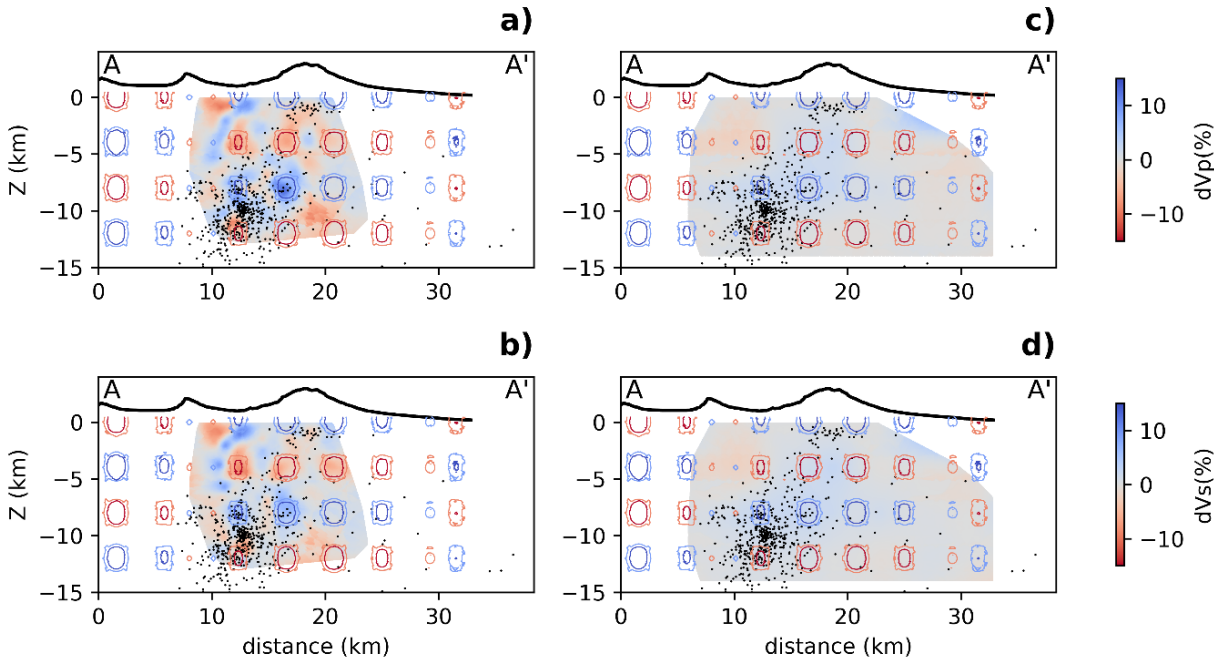



**Figure 5.** Results of the Shifted CKB synthetic test for the adaptive grid scheme (a and b) and the fixed grid scheme (c and d), for the parameters dVp (a and c) and dVs (b and d) respectively. The contour lines in each figure represent the synthetic checkerboard model used as a reference, with red indicating negative anomalies and blue indicating positive anomalies.

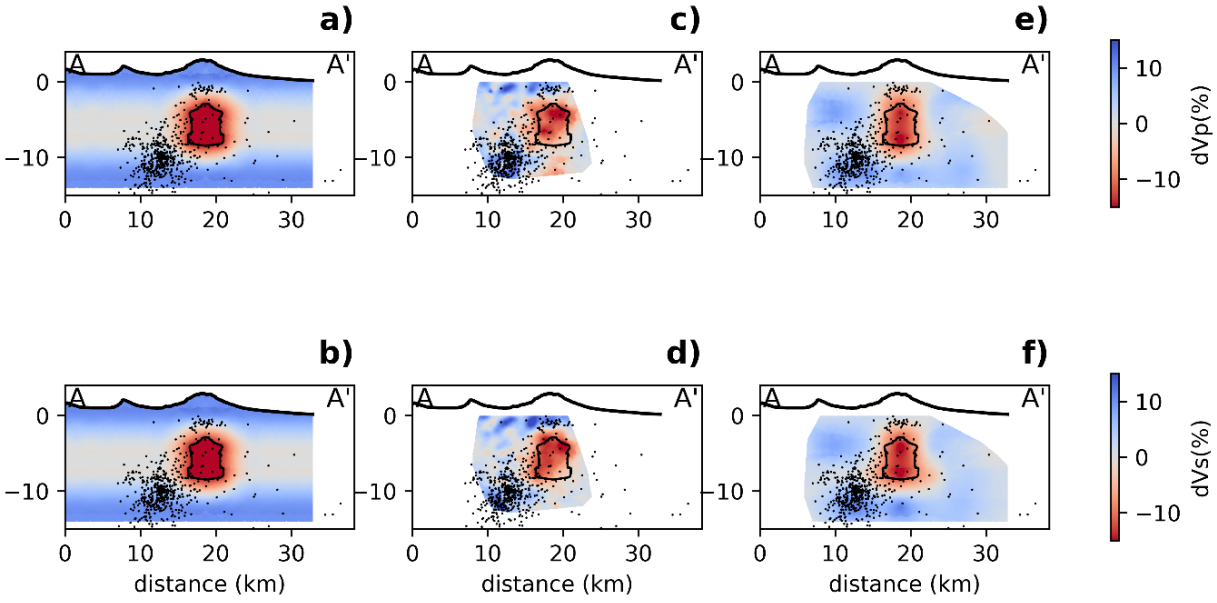



**Figure 6.** Synthetic test results for the low-velocity block model. (a) and (b) show the synthetic dVp and dVs models, (c) and (d) show the results of the dVp and dVs inversions using an adaptive grid scheme, (e) and (f) show the results of the dVp and dVs inversions using a fixed grid scheme.

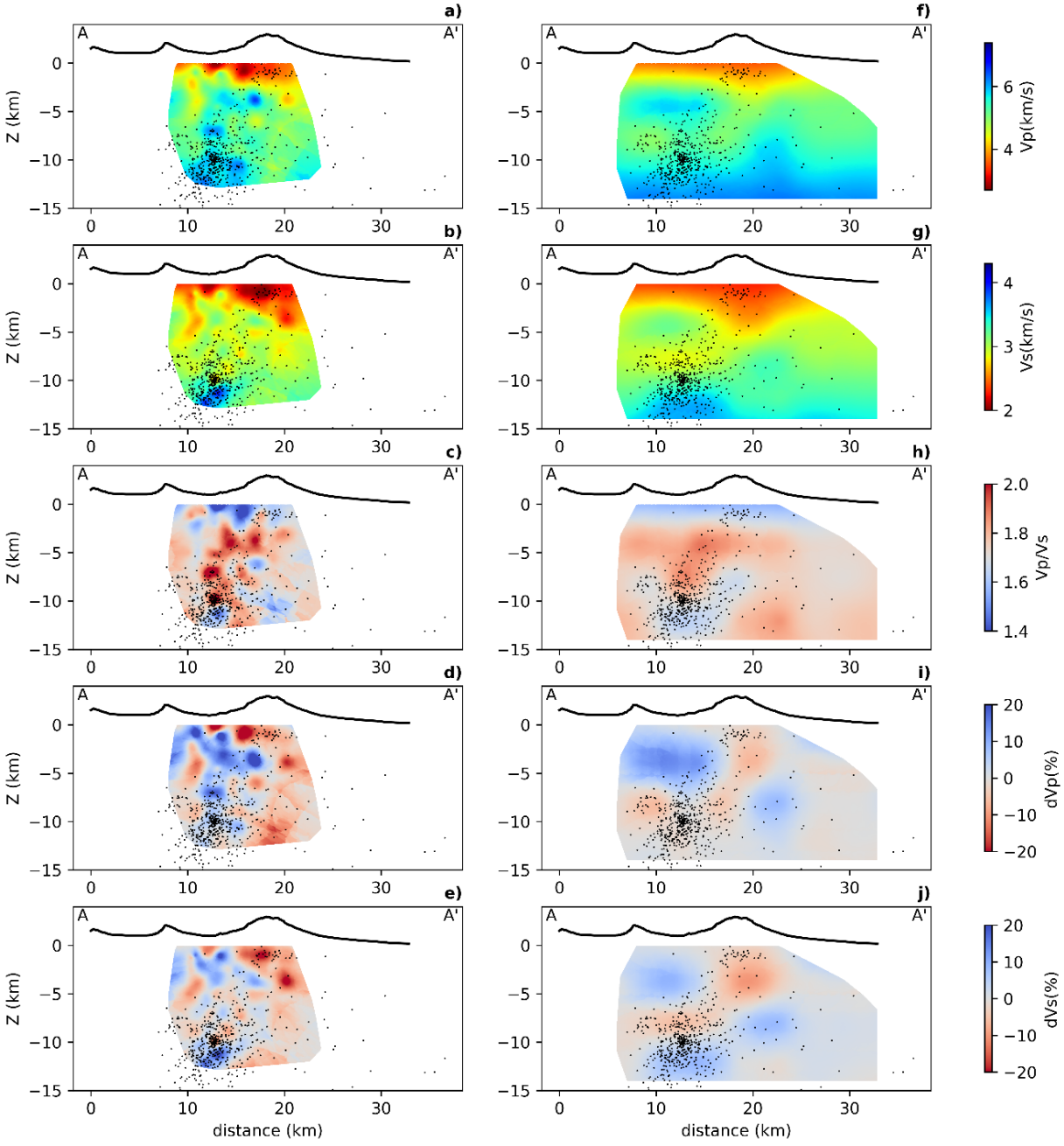



**Figure 7.** Results of synthetic tests on a complex model showing the parameters Vp, Vs, Vp/Vs, dVp and dVs, respectively, for the adaptive grid scheme (a-e) and the fixed grid scheme (f-j). The reference synthetic model used in these tests is shown on the left side of Fig. 10.

**Table 1.** A summary of the quantitative results for all synthetic test based on various evaluation matrices, in order to compare the performance of the adaptive grid and fixed grid schemes.

| Model | Data Missfit | Model Recovery | | | | | | Anomaly Recovery | | | | | |
|---|---|---|---|---|---|---|---|---|---|---|---|---|---|
| | RMSE (s) | Vp RMSC (km/s) | Vs RMSE (km/s) | Vp MAE (km/s) | Vs MAE (km/s) | Vp Correlation | Vs Correlation | dVp RMSE (%) | dVs RMSE (%) | dVp MAE (%) | dVs MAE (%) | dVp Correlation | dVs Correlation |
| CKB 1% (fixed) | 0.03538 | 0.13156 | 0.07646 | 0.08947 | 0.05206 | 0.97847 | 0.96075 | 2.67668 | 2.66802 | 1.81842 | 1.81112 | 0.39657 | 0.41164 |
| CKB 1% (adaptive) | 0.03299 | 0.15586 | 0.08599 | 0.11032 | 0.06084 | 0.96908 | 0.94961 | 3.25357 | 3.01089 | 2.27859 | 2.12584 | 0.26448 | 0.31401 |
| CKB 3% (fixed) | 0.07390 | 0.13304 | 0.07784 | 0.09005 | 0.05328 | 0.97759 | 0.95943 | 2.70212 | 2.70763 | 1.82899 | 1.84980 | 0.36454 | 0.38054 |
| CKB 3% (adaptive) | 0.07246 | 0.16070 | 0.09056 | 0.11543 | 0.06558 | 0.96665 | 0.94407 | 3.32209 | 3.16031 | 2.37015 | 2.28736 | 0.23278 | 0.28030 |
| Shifted CKB 1% (fixed) | 0.04245 | 0.16078 | 0.09293 | 0.10919 | 0.06308 | 0.96859 | 0.94316 | 3.22561 | 3.20959 | 2.20332 | 2.18408 | 0.01100 | 0.01085 |
| Shifted CKB 1% (adaptive) | 0.03371 | 0.16952 | 0.09074 | 0.12215 | 0.06524 | 0.96545 | 0.94624 | 3.65122 | 3.23838 | 2.56030 | 2.30583 | 0.23081 | 0.31180 |
| Shifted CKB 3% (fixed) | 0.07789 | 0.14862 | 0.08656 | 0.10403 | 0.06098 | 0.97240 | 0.94999 | 2.97324 | 2.98102 | 2.09646 | 2.10663 | 0.03337 | 0.02102 |
| Shifted CKB 3% (adaptive) | 0.07291 | 0.15912 | 0.08469 | 0.11791 | 0.06290 | 0.96756 | 0.95133 | 3.31228 | 2.97252 | 2.42719 | 2.19866 | 0.25286 | 0.33603 |
| Low velocity block 1% (fixed) | 0.03396 | 0.20390 | 0.11297 | 0.17607 | 0.09512 | 0.95858 | 0.93073 | 4.37281 | 4.12275 | 3.68515 | 3.39896 | 0.61796 | 0.67771 |
| Low velocity block 1% (adaptive) | 0.03464 | 0.20372 | 0.11588 | 0.15699 | 0.09086 | 0.94831 | 0.91259 | 3.97260 | 3.98226 | 3.13255 | 3.14702 | 0.71232 | 0.73058 |
| Low velocity block 3% (fixed) | 0.07248 | 0.20794 | 0.11919 | 0.17845 | 0.10196 | 0.95618 | 0.92187 | 4.43381 | 4.31373 | 3.72622 | 3.62444 | 0.60308 | 0.64187 |
| Low velocity block 3% (adaptive) | 0.07202 | 0.22957 | 0.11951 | 0.17383 | 0.09379 | 0.93273 | 0.90557 | 4.42832 | 4.10368 | 3.45109 | 3.24333 | 0.63559 | 0.71137 |
| Complex 1% (fixed) | 0.07438 | 0.50968 | 0.21775 | 0.38571 | 0.15833 | 0.76885 | 0.80702 | 10.86279 | 7.86911 | 8.01677 | 5.60627 | 0.35665 | 0.34079 |
| Complex 1% (adaptive) | 0.05340 | 0.32863 | 0.13569 | 0.24560 | 0.09721 | 0.91070 | 0.92979 | 6.89241 | 4.76042 | 5.07727 | 3.40292 | 0.81048 | 0.81859 |
| Complex 3% (fixed) | 0.09816 | 0.51429 | 0.21892 | 0.38973 | 0.15825 | 0.76492 | 0.80577 | 10.93189 | 7.90800 | 8.08650 | 5.60422 | 0.34387 | 0.33477 |
| Complex 3% (adaptive) | 0.08386 | 0.34690 | 0.14529 | 0.26019 | 0.10480 | 0.89794 | 0.91835 | 7.26779 | 5.07828 | 5.37470 | 3.66285 | 0.78101 | 0.78861 |

## 3.2 Real Data Inversion

For the real data inversion, two distinct schemes were implemented. The first scheme employed a fixed grid discretization with uniform 3 km × 3 km × 4 km dimensions. The size of 3 × 3 × 4 km is the optimal grid size from previous tomography studies (Ardianto et al., 2021) using the same data. The second scheme incorporated the previously described adaptive grid methodology, initialized at identical starting dimensions (3 km × 3 km × 4 km). In this inversion process, we use an intermediate grid with uniform spatial dimensions of 0.5 km × 0.5 km × 0.5 km. We then limit the distance between inversion grid nodes to no less than the size of the intermediate grid. For the adaptive grid scheme, the threshold value is determined through trial and error to achieve sufficiently even distribution of RHC in all grids. After applying the adaptive scheme, the distribution of nodes that construct the Voronoi grid becomes more concentrated in areas with high raypath density, as shown in Fig. 8.

The adaptive grid scheme increased the mean RHC from 190 to 236 while reducing its standard deviation from 485 to 224. This increase in the mean and reduction in the standard deviation indicate that the adaptive scheme is capable of effectively reducing the variability of the RHC distribution. Figure 9 also visually confirms this, comparing the RHC distributions between the adaptive scheme and the fixed grid scheme. With the adaptive scheme, no single grid-node has a significantly higher number of raypaths than the others, resulting in a more balanced and homogeneous distribution of rays across each grid element. In the fixed grid scheme, the RMS

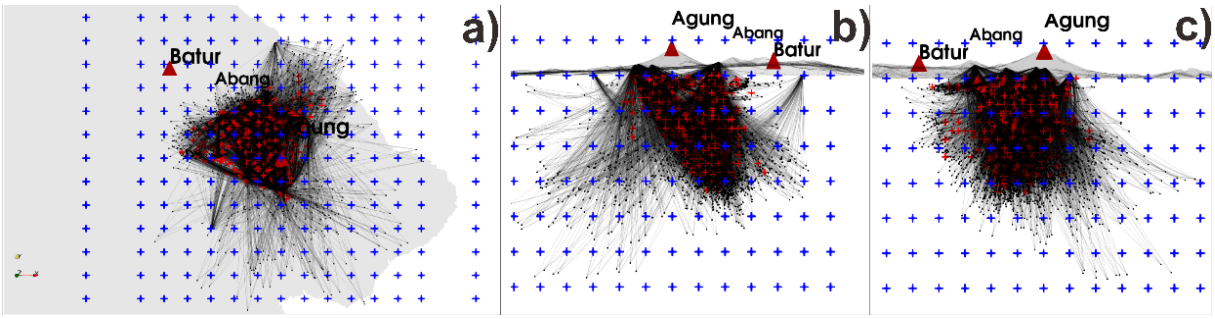



**Figure 8.** The position of nodes used to construct the Voronoi grid before (blue '+') and after (red '+') applying the adaptive scheme. (a) map view, (b) looking to west, (c) looking to north.

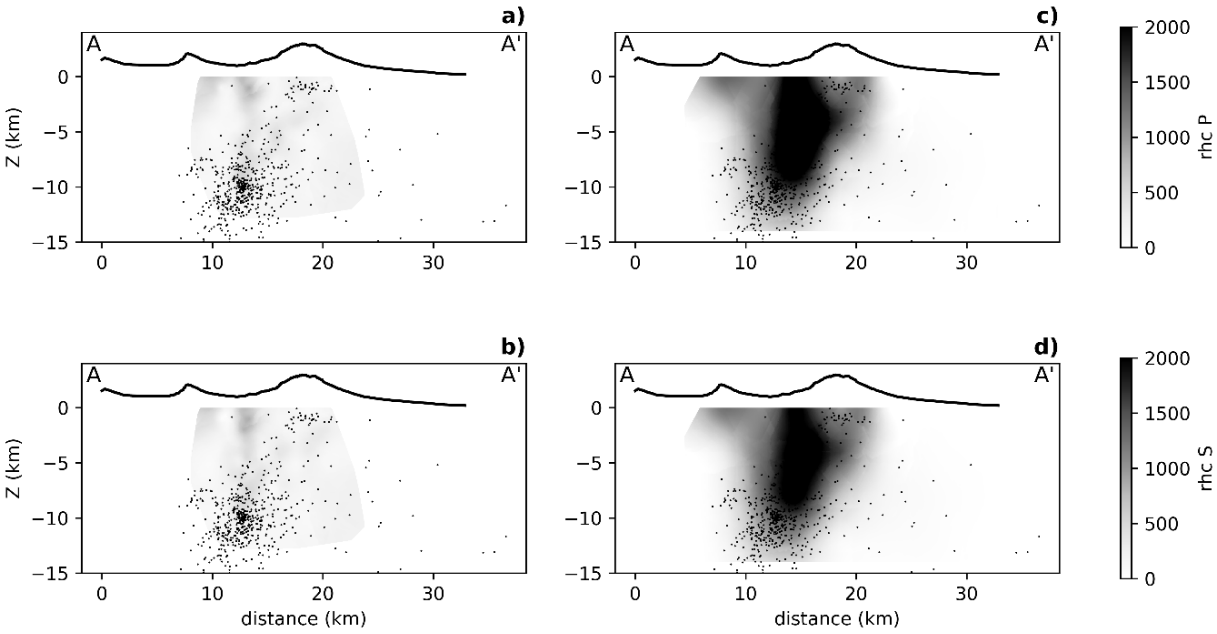



**Figure 9.** Distribution of RHC values for the P-wave (top) and S-wave (bottom) in the adaptive grid scheme (left: a and b) and the fixed grid scheme (right: c and d).

residual decreased from 0.23358 s to 0.1830 s, while the adaptive grid scheme performed better with a final RMS residual of 0.15344 s.

The real-data inversion results are presented in Fig. 10, revealing four distinct anomalous regions from both schemes: Area 1: An area showing high seismicity at ~10 km depth, situated at the boundary between high and low dVp and dVs anomaly. Area 2: An area showing moderately low dVp, low dVs and high Vp/Vs ratios (with absolute Vp = 4.8 – 6.5 km/s and Vs = 2.5 – 3.0 km/s). Area 3: An area showing high dVp and dVs with high Vp/Vs ratios (with absolute Vp = 5.5 – 7.0 km/s and Vs = 2.8 – 4.0 km/s). Area 4: An area showing moderately low dVp, low dVs, and high Vp/Vs ratios (with absolute Vp = 3.2 – 4.7 km/s and Vs = 2.0 – 2.5 km/s). Although all four anomalies can be identified in both schemes, Fig. 10 shows that the dimensions and spatial positions of the anomalies produced by each scheme are not entirely the same.

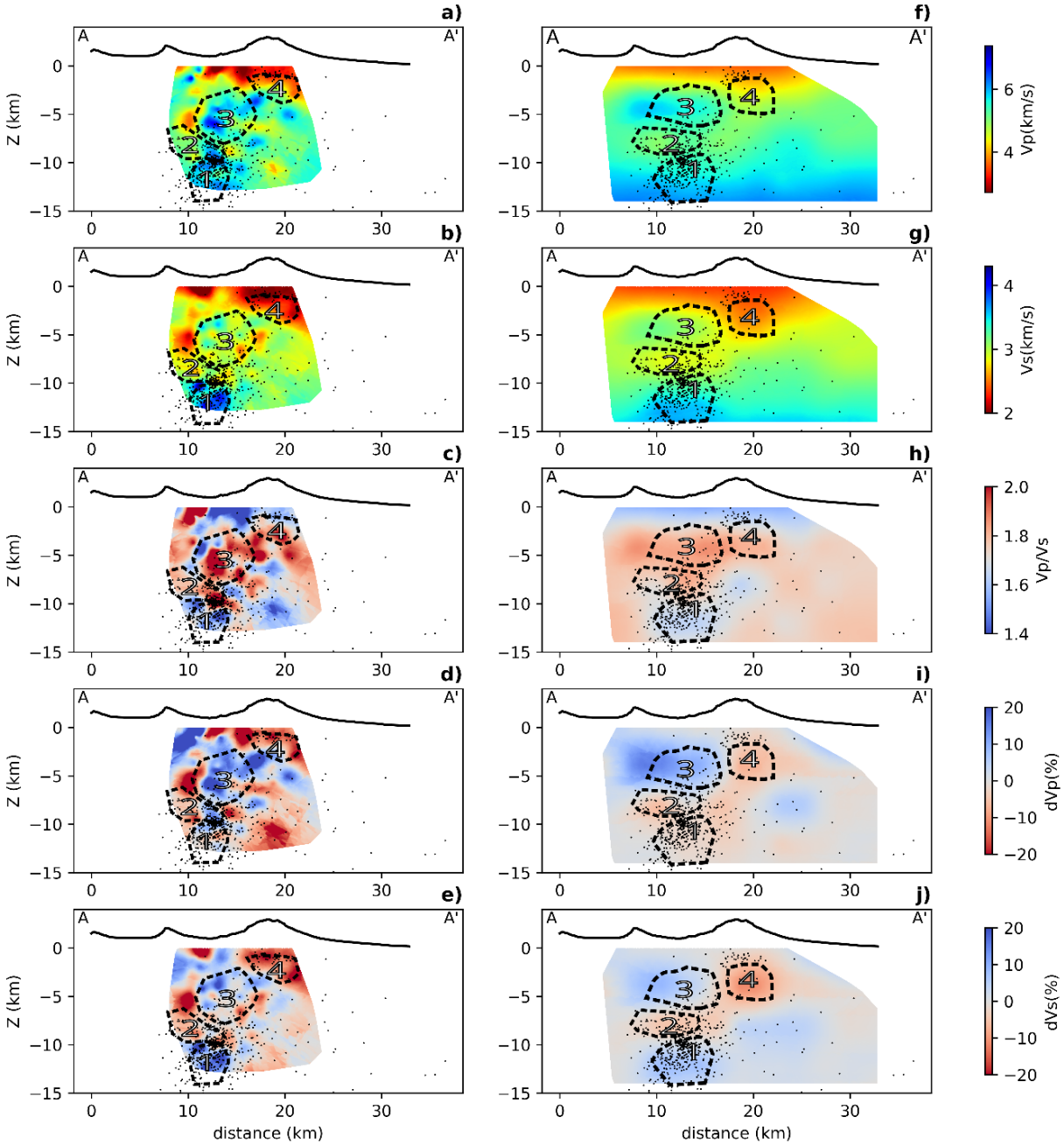



**Figure 10.** Results of real data inversion for the adaptive grid scheme (a-e) and the fixed grid scheme (f-j). Each shows the distribution of Vp (a, f), Vs (b, g), Vp/Vs (c, h), dVp (d, i) and dVs (e, j). There are four anomaly areas, which are described in the text.

## 3.3 Discussion

The first synthetic test on the standard CKB model showed that both adaptive and fixed grid scheme were able to reconstruct the synthetic model effectively. Qualitatively, the fixed-grid scheme exhibited a high degree of pattern agreement with the synthetic model, as expected, since the geometry of the anomaly in this test was designed to align with the fixed grid size used. However, the results in Fig. 4 show that the adaptive grid scheme is also capable of adequately representing the distribution of high and low velocity anomalies, even with a sharper contrast between the anomalies compared to the fixed grid scheme. Quantitatively, the summary of evaluation metrics in Table 1 indicates that the performance of the two schemes is relatively comparable, with the fixed-grid scheme showing only a slight advantage over the adaptive-grid scheme.

In the second synthetic test, which is the CKB model with positive and negative anomalies deliberately misaligned with the inversion grid nodes, the advantages of the adaptive grid scheme was noticeable. The fixed-grid scheme failed to reconstruct the chessboard-like anomaly pattern, whilst the adaptive-grid scheme was still able to capture it well, as shown in Fig. 5. This advantage is confirmed by the quantitative data in Table 1, which shows that the adaptive-grid scheme produces significantly higher correlation values for dVp and dVs compared to the fixed-grid scheme. Similar results are also observed in the third test (the low-velocity block model), where the adaptive grid scheme consistently exhibits higher correlation values and lower error rates (Table 1). As shown in Fig. 6, the fixed grid scheme produces a smoother model whilst still adequately representing the low-velocity anomalies. Furthermore, the adaptive scheme performs better at reconstructing high-velocity anomalies located above the low-velocity block, whilst maintaining background values (no anomalies) in the areas to the left and right of the block in accordance with the synthetic model. In contrast, the fixed-grid scheme produces high-velocity anomalies in areas where no anomalies should be present.

The last synthetic test was carried out on a complex model constructed based on the results of an adaptive grid inversion (Fig. 10) as a reference synthetic model. In this test, the adaptive grid scheme was able to reconstruct the model well, as indicated by low error values and high correlation coefficients, both for the absolute velocity (Vp and Vs) and for the relative perturbations (dVp and dVs). Conversely, the fixed-grid scheme with a relatively coarse grid-node size ($3 \times 3 \times 4$ km) was unable to capture the variations in anomalies properly. This limitation in spatial resolution meant that the fixed-grid scheme failed to represent the complexity and spatial detail of the synthetic model under test, given that the variations in anomalies in the reference model were far finer than the discretisation capability of the fixed grid.

Overall, all the synthetic test scenarios conducted show that both the adaptive and fixed grid schemes are capable of reconstructing the synthetic model well. This indicates that the inversion algorithms used have a good numerical reliability and robustness. Nevertheless, differences in reconstruction quality are evident in the spatial resolution produced. The adaptive grid scheme proved capable of sharpening the boundaries of anomalies more distinctly, whilst the fixed grid scheme tended to produce smoother models, meaning that the contrast between anomalies was not mapped as well as with the adaptive scheme. However, artefacts are still detected at several points, indicating the limitations of the grid adaptation method, which is based solely on the RHC value. The findings indicate the need to integrate additional parameters, such as raypath orientation distribution, in determining the grid adaptation threshold for more comprehensive optimisation (Kissling, 1988; Sambridge and Faletič, 2003; Zhang and Thurber, 2005).

Synthetic tests on the final model confirmed that the results of real-data inversion using the adaptive-grid scheme demonstrated reliable performance. Furthermore, synthetic tests for the fixed-grid scheme showed strong alignment with the results of real-data inversion using the same scheme. The stability of these inversion results is further supported by synthetic tests involving the addition of 1% and 3% noise, which were found not to significantly reduce the quality of the model reconstruction. Consequently, the anomalies identified in Fig. 10 are considered robust and reliable for geological interpretation. The four anomalies that have been identified will be discussed in further detail by relating them to the phases of the 2017 Agung Volcano eruption based on previous studies (Syahbana et al., 2019).

The first phase occurred between March and September 2017. The increase in magma activity in this phase is characterized by the presence of several seismic events between the Agung and Batur volcanoes and inflationary signals in the GNSS data (Albino et al., 2019; Syahbana et al., 2019). Unfortunately, our tomograms are only able to recover to a depth of ~13 km, so we are still unable to model the position and dimensions of the deep reservoir, which, from previous modelling, lies at a depth of approximately 20 km. Moreover, it is still unclear if a mid-reservoir exists along the crust-mantle border at a depth of approximately 14-15 km, limiting the depth of magma movement in the first phase to that depth.

The next phase is the presence of a dyke intrusion in the area between Agung Volcano and Mount Abang (Ardianto et al., 2021; Syahbana et al., 2019). This phase was characterized by significant seismicity around Area 1 from late September to October 2017. This phase was followed by dyke intrusion in the area between Mount Agung and Mount Batur. The presence of this intrusion has been successfully modelled and validated using InSAR data in previous studies (Albino et al., 2019). We identify Area 2, located at depths of 7.5-10 km, as the dyke intrusion zone. It is characterized by moderately low Vp, low Vs, and high Vp/Vs (>1.7), with these anomaly values reflecting high temperatures due to the dyke intrusion. Several studies that have been conducted have shown that an increase in temperature can cause a decrease in the values of Vp and Vs, as well as an increase in the value of Vp/Vs (Kampfmann and Berckhemer, 1985; Mizutani and Kanamori, 1964; Murase and McBIRNEY, 1973; Sanders et al., 1995; Sato et al., 1989; Sato and Sacks, 1989; Stocker and Gordon, 1975). Area 2 was identified at a depth of 7.5-10 km, which is slightly different from that indicated by previous tomography studies (8-14 km) (Ardianto et al., 2021). By comparison, InSAR modelling indicates that the dyke intrusion lies at depths ranging from 7 to 13 km (Albino et al., 2019), whilst gravity-magnetic modelling places it at depths of 5-11 km (Suryanata et al., 2024). There is a possibility that the dyke intrusion we marked extends to the area below Mount Batur, corresponding to the schematic model of the subsurface structure using magnetic and gravity data in the Bali area (Suryanata et al., 2024). However, we cannot confirm this because the resolution in the Batur area is not well covered.

Previous study suggest that there is a barrier (stiffer layer) that prevents the upward migration of magma and caused the October 2017 event to be suspended at a depth of 6 km (Sahara et al., 2021). We interpret that the layer in question is the Area 3 area from our tomogram results, which has high Vp, high Vs, high Vp/Vs, and is found at a depth of 2.5-7.5 km. The stiffer layer is likely composed of older strong volcanic rocks, similar to the anomalies found in the Sinabung Volcano (Nugraha et al., 2019), which has high dVp, dVs, and Vp/Vs anomalies. There is also a high-velocity anomaly at Augustine volcano, Alaska, which is considered to be a conduit from a past eruption (Syracuse et al., 2011).

The last phase is the rise of magma in the shallow reservoir. This phase occurred between the early- and mid-November periods (before the first eruption) and is characterized by a change in seismicity from volcanic tectonics to low-frequency (LF) and tremors. In this shallow reservoir, mixing occurs between mafic magma from the intrusion and more differentiated magma that already exists in the shallow reservoir. Area 4 is what we considered to be a shallow reservoir. The moderately low Vp, low Vs, and high Vp/Vs in Area 4 are the result of high temperatures caused by magmatic activity. This is in line with the interpretation of tomography studies at Merapi Volcano (Widiyantoro et al., 2018), where there are low dVp and high Vp/Vs values at depths of less than 4 km, which are identified as shallow reservoirs. Area 4 was identified at a depth of 1 to 3 km relative to sea level.

Previous study (Ardianto et al., 2021) suggest that the shallow reservoir area was represented as a high Vp anomaly. However, high-temperature melt should be represented as a zone with a relatively low velocity. Furthermore, the shallow reservoir in previous tomography studies was found at relatively shallow depths, between −2 and 2 km. Several previous studies have identified the location of the shallow reservoir at varying depths. Geiger et al. (2018) located it at depths of 3-7 km based on thermobarometric and isotope data, Chaussard and Amelung (2012) modelled it at depths of 2-4 km using InSAR data, while Suryanata et al. (2024) obtained depth of 4 – 7 km using magnetic and gravity data. When compared with the results of this study, which locates the shallow reservoir at a depth of 1-3 km, this position appears more appropriate and closer to that of other models. Furthermore, the area we have identified as the shallow reservoir also has a relatively low Vp value, which is more consistent with the expected presence of high-temperature melt.

The four anomaly zones (Areas 1-4) were consistently detected in both the constant and adaptive grid schemes. However, there were significant differences in their dimensions and spatial location. The adaptive grid scheme produced higher spatial resolution than the fixed grid, manifested in a more detailed representation of anomalies. In the adaptive grid, a single anomaly can be represented by many small grid cells, while the constant grid can only represent a single anomaly through one or several large grid cells. This increase in spatial resolution enables more precise delineation of anomaly boundaries and the construction of a more precise schematic diagram of the magma flow beneath Agung Volcano. The visualisation of the combined isosurface of dVp, dVs, and Vp/Vs ratio anomalies in Fig. 11 successfully reconstructed the three-dimensional geometry of the magma body and its flow pattern during the 2017 eruption phase. Intrusion zones and shallow reservoirs were identified through Vp/Vs values >1.7 combined with dVs values <−5% in the adaptive grid scheme, while in the fixed grid scheme, dVs values <−4% were used. Meanwhile, stiffer rock zones were identified through dVp and dVs values >5% in the adaptive grid scheme, and >1% in the fixed grid scheme. The difference in cut-off values was due to the fact that in the fixed grid scheme, the anomaly results were smoother than those from the adaptive grid scheme.

Based on the isosurface plot visualisation, it can be observed that the representation of shallow reservoir volumes in the adaptive grid scheme is more detailed and naturally varying due to denser grid-node distribution. On the other hand, the interpretation results of the intrusion zone in the fixed grid scheme show a more rigid geometry. However, the fixed grid scheme still has the advantage of producing a simpler and smoother model, thus providing a stable overview for initial interpretation. Therefore, in local passive seismic tomography studies, especially for volcanic environments, we recommend a hybrid approach that combines both schemes. The implementation stages include: (1) applying a fixed grid scheme with grid size optimised through the resolution test to obtain a general overview of the anomalies, and (2) applying an adaptive grid scheme to improve the sharpness, detail and precision of the model based on the initial results obtained. This hierarchical strategy allows for the acquisition of models that simultaneously maintain the stability of general interpretations and the resolution of details in complex zones.

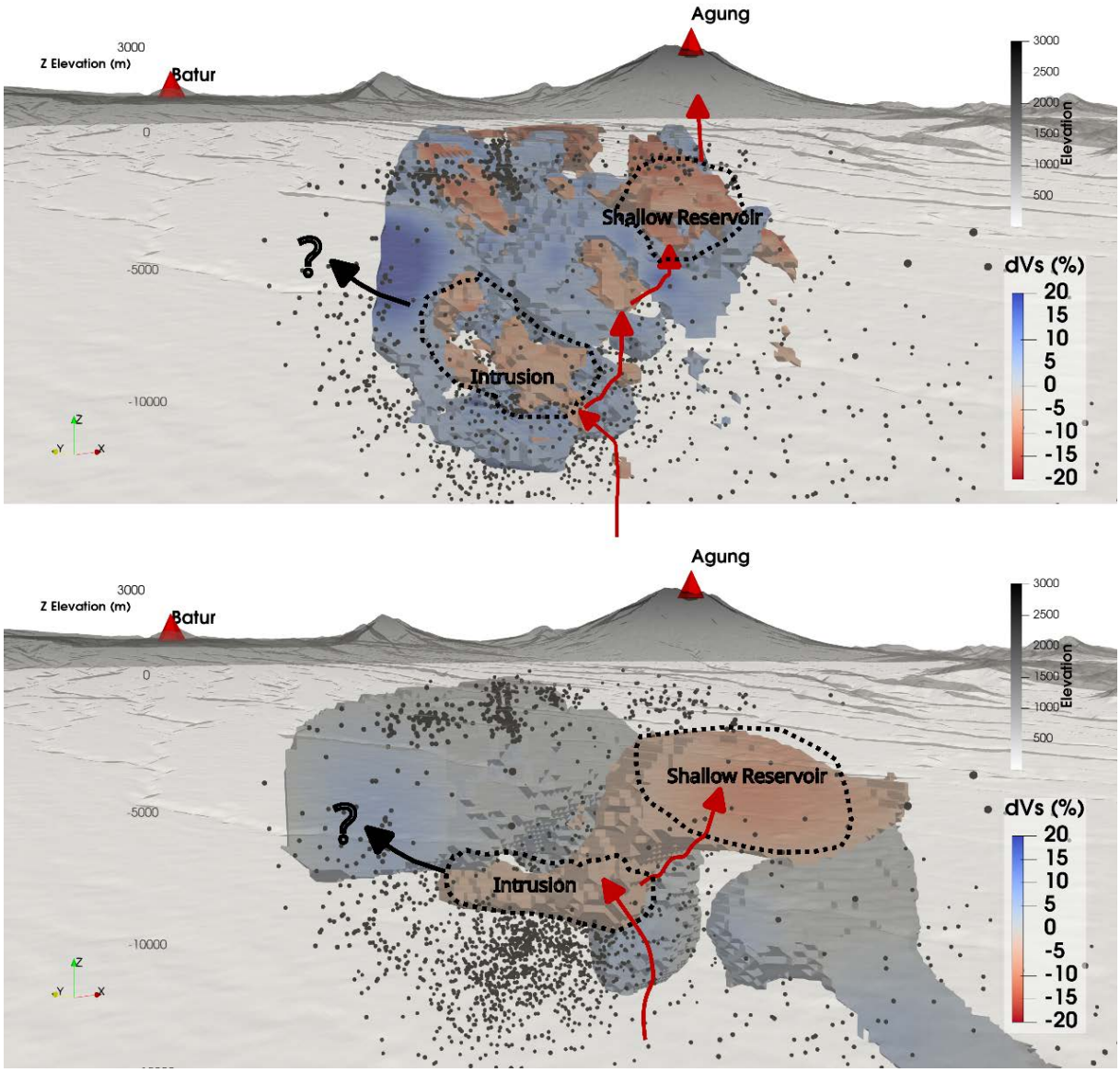



**Figure 11.** 3D isosurface visualisation of the combination of dVp, dVs, and the Vp/Vs ratio using an adaptive grid scheme (top) and a fixed grid scheme (bottom). This model reconstructs magmatic bodies and pathways during the 2017 eruption of Agung Volcano. The difference structural complexity between the two schemes is evident, with the adaptive grid showing sharper geometric details. The cut-off values for each parameter are explained in the discussion section.

## 4. Conclusion

Based on the studies conducted, the implementation of two grid parameterisation schemes adaptive grid and fixed grid in tomography inversion at Agung Volcano shows that the adaptive grid scheme produces better performance. The adaptive grid scheme is carried out by dynamically adding or removing grid nodes based on the distribution of Ray Hit Count (RHC) at each node. Synthetic test results confirm this improvement, with the adaptive grid scheme consistently capable of reconstructing complex anomalies more effectively. The inversion results of real-data inversion with adaptive grid scheme produce a lower RMS residual, sharper seismic velocity anomalies, and improved spatial resolution due to higher grid node density. This facilitates more precise delineation of subsurface structures, particularly in reconstructing the magmatic system beneath Agung Volcano.

However, this adaptive approach still requires refinement in terms of determining threshold parameters for automatic grid-node placement optimisation. In this study, the adaptation threshold still refers to the optimal grid size from previous studies based on the Checkerboard Resolution Test (CRT), which was then modified based on the distribution of Ray Hit Count (RHC) values per grid node. The synthetic test results still show artefact anomalies in some areas that cannot be optimally reconstructed. Therefore, it is necessary to develop a more comprehensive threshold parameter justification, such as considering the orientation and azimuth distribution of raypaths passing through each grid node, rather than relying solely on the number of rays. This multidimensional approach is expected to improve the accuracy of model resolution and reduce the occurrence of artefacts in inversion.

We recommend the application of a hybrid approach in local passive seismic tomography that integrates fixed grid and adaptive grid schemes. The fixed grid scheme (whose grid size is optimised through synthetic tests such as the Checkerboard Resolution Test) plays a role in providing a general and stable overview of the distribution of velocity anomalies. Subsequently, an adaptive grid scheme is applied to improve spatial resolution in more complex areas. This combination allows for the derivation of a model that simultaneously maintains the consistency of general interpretation and the sharpness of detail in geological features that require high resolution.

**Data availability statement.** The dataset is available from the corresponding author upon reasonable request at i.puturaditya@upnyk.ac.id. The code is available on the GitHub repository https://github.com/radityaambara/PyLIGTomo.git; for further information please contact: i.puturaditya@upnyk.ac.id.

**Acknowledgements.** The figures were generated with Matplotlib in Python and Paraview (https://www.paraview.org/) (Ahrens et al., 2005; Johnson and Hansen, 2005). All mathematical calculations were performed in the Python using the NumPy (Harris et al., 2020), SciPy (Virtanen et al., 2020), and Pandas (McKinney, 2010) modules.

## References

Abers, G. A. and S. W. Roecker (1991). Deep structure of an arc-continent collision: Earthquake relocation and inversion for upper mantle P and S wave velocities beneath Papua New Guinea. J. Geophys. Res., 96, 6379-6401, doi:10.1029/91JB00145.

Ahrens, J., B. Geveci and C. Law (2005). ParaView: An End-User Tool for Large-Data Visualization, in: Visualization Handbook. Elsevier, 717-731, doi:10.1016/B978-012387582-2/50038-1.

Albino, F., J. Biggs and D. K. Syahbana (2019). Dyke intrusion between neighbouring arc volcanoes responsible for 2017 pre-eruptive seismic swarm at Agung. Nat Commun 10. doi:10.1038/s41467-019-08564-9.

Amoroso, O., G. Festa, P. Bruno, L. D'Auria et al. (2018). Integrated tomographic methods for seismic imaging and monitoring of volcanic caldera structures and geothermal areas, J. Appl. Geophys., 156, 16-30.

Ardianto, A., A. D. Nugraha, H. Afif, D. K. Syahbana et al. (2021). Imaging the Subsurface Structure of Mount Agung in Bali (Indonesia) Using Volcano-Tectonic (VT) Earthquake Tomography, Front. Earth Sci., 9, doi:10.3389/feart.2021.619587.

Bai, C. and S. Greenhalgh (2005). 3D multi-step travel time tomography: Imaging the local, deep velocity structure of Rabaul volcano, Papua New Guinea, Phys. Earth Planet. Int., 151, 259-275, doi:10.1016/j.pepi.2005.03.009.

Battaglia, J., A. Zollo, J. Virieux and D. Dello Iacono (2008). Merging active and passive data sets in traveltime tomography: The case study of Campi Flegrei caldera (Southern Italy). Geophysical Prospecting 56, 555-573, doi:10.1111/j.1365-2478.2007.00687.x.

Böhm, G., P. Galuppo and A. Vesnaver (2000). 3D adaptive tomography using Delaunay triangles and Voronoi polygons, Geophys. Prospect., 48, 723-744, doi:10.1046/j.1365-2478.2000.00211.x.

Calo, M., C. Dorbath, D. Luzio, S. Rotolo and G. D'Anna (2009). Local earthquake tomography in the southern Tyrrhenian region of Italy: Geophysical and petrological inferences on the subducting lithosphere, 85-99.

Calo, M., L. Parisi and D. Luzio (2013). Lithospheric P- and S-wave velocity models of the Sicilian area using WAM tomography: procedure and assessments, Geophys. J. Int., 195, 625-649, doi:10.1093/gji/ggt252.

Chaussard, E. and F. Amelung (2012). Precursory inflation of shallow magma reservoirs at west Sunda volcanoes detected by InSAR, Geophys. Res. Lett., 39, 2012GL053817, doi:10.1029/2012GL053817.

Chiarabba, C. and A. Amato (2003). $V_p$ and $V_p/V_s$ images in the $M_w$ 6.0 Colfiorito fault region (central Italy): A contribution to the understanding of seismotectonic and seismogenic processes. J. Geophys. Res., 108, 2001JB001665, doi:10.1029/2001JB001665.

Curtis, A. and R. Snieder (1997). Reconditioning inverse problems using the genetic algorithm and revised parameterization, Geophysics, 62, 1524-1532, doi:10.1190/1.1444255.

Dobretsov, N., I. Y. Koulakov, K. Litasov and E. Kukarina (2015). An integrate model of subduction: contributions from geology, experimental petrology, and seismic tomography, Russian Geology and Geophysics 56, 13-38.

Eberhart-Phillips, D. (1990). Three-dimensional *P* and *S* velocity structure in the Coalinga Region, California. J. Geophys. Res., 95, 15343-15363, doi:10.1029/JB095iB10p15343.

Eberhart-Phillips, D. and A. J. Michael (1998). Seismotectonics of the Loma Prieta, California, region determined from three-dimensional $V_p$, $V_p/V_s$, and seismicity, J. Geophys. Res., 103, 21099-21120, doi:10.1029/98JB01984.

Fang, H., M. C. A. White, Y. Lu and Y. Ben-Zion (2022). Seismic Traveltime Tomography of Southern California Using Poisson-Voronoi Cells and 20 Years of Data, J. Geophys. Res.: Solid Earth 127, e2021JB023307, doi:10.1029/2021JB023307.

Foix, O., C. Aiken, J.-M. Saurel, N. Feuillet et al. (2021). Offshore Mayotte volcanic plumbing revealed by local passive tomography, J. Volcanol. Geoth.Res., 420, 107395, doi:10.1016/j.jvolgeores.2021.107395.

Garcia, V. V., M. Calò and J. F. L. Samaniego (2019). Imaging of the magmatic system feeding Las Tres Virgenes Geothermal field (Baja California Sur, Mexico) using Enhanced Seismic Tomography, J. Volcanol. Geoth. Res., 388, 106710.

Geiger, H., V. R.Troll, E. M. Jolis, F. M.Deegan et al. (2018). Multi-level magma plumbing at Agung and Batur volcanoes increases risk of hazardous eruptions, Sci. Rep., 8, 10547, doi:10.1038/s41598-018-28125-2.

Harris, C. R., K. J. Millman, S. J. Van Der Walt, R. Gommers et al. (2020). Array programming with NumPy. Nature 585, 357-362, doi:10.1038/s41586-020-2649-2.

Heath, B. A., E. E. E. Hooft, D. R. Toomey and M. J. Bezada (2015). Imaging the magmatic system of Newberry Volcano using joint active source and teleseismic tomography, Geochem. Geophys. Geosyst., 16, 4433-4448, doi:10.1002/2015GC006129.

Hidayat, W., D. P. Sahara, S. Widiyantoro, S. Suharsono et al. (2024). 4D time lapse tomography for monitoring cave propagation and stress distribution in Deep Mill Level Zone (DMLZ) PT Freeport Indonesia, Geomech. Geophys. Geo-energ. Geo-resour, 10, 39, doi:10.1007/s40948-023-00718-w.

Johnson, C. R. and C. D. Hansen (Eds.) (2005). The visualization handbook. Academic, Oxford.

Jousset, P., R. Sule, W. Diningrat, D. K. Syahbana et al. (2015). Seismic tomography and monitoring of magmatic geothermal and natural hydrothermal systems in the south of Bandung, Indonesia, Presented at the World Geothermal Congress 2015.

Kamath, G., L. Shi, E. Chow and W.-Z. Song (2016). Distributed Tomography with Adaptive Mesh Refinement in Sensor Networks, Int.J.Sensor Networks, 23, 1, 40-52, doi:10.1504/IJSNET.2017.080604.

Kampfmann, W. and H. Berckhemer (1985). High temperature experiments on the elastic and anelastic behaviour of magmatic rocks, Phys. Earth Planet. Int., 40, 223-247, doi:10.1016/0031-9201(85)90132-3.

Kissling, E. (1988). Geotomography with local earthquake data, Rev. Geophys., 26, 659-698, doi:10.1029/RG026i004p00659.

Kissling, E., W. L. Ellsworth, D. Eberhart-Phillips and U. Kradolfer (1994). Initial reference models in local earthquake tomography, J. Geophys. Res., 99, 19635-19646, doi:10.1029/93JB03138.

Kissling, E., U. Kradolfer and H. Maurer (1995). Velest User's Guide. Int. Inst. Geophys., 1-26.

Koulakov, I. (2009). LOTOS Code for Local Earthquake Tomographic Inversion: Benchmarks for Testing Tomographic Algorithms, Bull. Seismol. Soc. Am., 99, 194-214, doi:10.1785/0120080013.

Koulakov, I., A. Jakovlev and B. G. Luehr (2009). Anisotropic structure beneath central Java from local earthquake tomography, Geochem. Geophys, Geosyst., 10, 2008GC002109, doi:10.1029/2008GC002109.

Koulakov, I. Y. (2022). Seismic tomography of Kamchatkan volcanoes, Russian Geology and Geophysics 63, 1207-1244.

Lees, J. M. (2007). Seismic tomography of magmatic systems, J. Volcanol. Geotherm. Res., 167, 37-56.

Lomax, A., J. Virieux, P. Volant and C. Berge-Thierry (2000). Probabilistic Earthquake Location in 3D and Layered Models, in: Thurber, C.H., Rabinowitz, N. (Eds.), Advances in Seismic Event Location, Modern Approaches in Geophysics. Springer Netherlands, Dordrecht, 101-134, doi:10.1007/978-94-015-9536-0_5.

Luxbacher, K., E. Westman, P. Swanson and M. Karfakis (2008). Three-dimensional time-lapse velocity tomography of an underground longwall panel, Int. J. Rock Mech. Minin. Sci., 45, 478-485, doi:10.1016/j.ijrmms.2007.07.015.

McKinney, W. (2010). Data Structures for Statistical Computing in Python. Presented at the Python in Science Conference, Austin, Texas, 56-61, doi:10.25080/Majora-92bf1922-00a.

Mercier, J.-P., W. De Beer, J.-P. Mercier and S. Morris (2015). Evolution of a block cave from time-lapse passive source body-wave traveltime tomography. Geophysics 80, WA85-WA97, doi:10.1190/geo2014-0155.1.

Michelini, A. (1995). An adaptive-grid formalism for traveltime tomography, Geophys. J. Int., 121, 489-510, doi:10.1111/j.1365-246X.1995.tb05728.x.

Mizutani, H. and H. Kanamori (1964). Variation of Elastic Wave Velocity and Attenuative Property near the Melting Temperature. J. Phys. Earth 12, 43-49, doi:10.4294/jpe1952.12.43.

Murase, T. and A. R. McBirney (1973). Properties of Some Common Igneous Rocks and Their Melts at High Temperatures, Geol Soc. Am. Bull., 84, 3563, doi:10.1130/0016-7606(1973)84%3C3563:POSCIR%3E2.0.CO;2.

Neri, G., B. Orecchio, C. Totaro, G. Falcone and D. Presti (2009). Subduction beneath southern Italy close the ending: Results from seismic tomography. Seismological Research Letters 80, 63-70.

Nolet, G. (2023). Path-averaged delay times for seismic tomography, Geophys. J. Int., 235, 996-1005, doi:10.1093/gji/ggad282.

Nugraha, A. D., N. Indrastuti, R. Kusnandar, H. Gunawan et al. (2019). Joint 3-D tomographic imaging of Vp, Vs and Vp/Vs and hypocenter relocation at Sinabung volcano, Indonesia from November to December 2013, J. Volcanol. Geoth. Res., 382, 210-223, doi:10.1016/j.jvolgeores.2017.09.018.

Paige, C. C. and M. A. Saunders (1982a). Algorithm 583: LSQR: Sparse Linear Equations and Least Squares Problems, ACM Trans. Math. Softw., 8, 195-209, doi:10.1145/355993.356000.

Paige, C. C. and M. A. Saunders (1982b). LSQR: An Algorithm for Sparse Linear Equations and Sparse Least Squares, ACM Trans. Math. Softw., 8, 43-71, doi:10.1145/355984.355989.

Qian, J., H. Zhang and E. Westman (2018). New time-lapse seismic tomographic scheme based on double-difference tomography and its application in monitoring temporal velocity variations caused by underground coal mining, Geophys. J. Int., 215, 2093-2104, doi:10.1093/gji/ggy404.

Replumaz, A., A. M. Negredo, S. Guillot and A. Villaseñor (2010). Multiple episodes of continental subduction during India/Asia convergence: Insight from seismic tomography and tectonic reconstruction, Tectonophysics 483, 125-134.

Sahara, D. P., P. P. Rahsetyo, A. D. Nugraha, D. K. Syahbana et al. (2021). Use of Local Seismic Network in Analysis of Volcano-Tectonic (VT) Events Preceding the 2017 Agung Volcano Eruption (Bali, Indonesia), Front. Earth Sci., 9, 619801, doi:10.3389/feart.2021.619801.

Sambridge, M. and R. Faletič (2003). Adaptive whole Earth tomography. Geochem Geophys Geosyst, 4, 2001GC000213, doi:10.1029/2001GC000213.

Sambridge, M. and N. Rawlinson (2005). Seismic tomography with irregular meshes, in: Levander, A., Nolet, G. (Eds.), Geophysical Monograph Series. American Geophysical Union, Washington, D. C., 49-65, doi:10.1029/157GM04.

Sanders, C. O., S. C. Ponko, L. D. Nixon and E. A. Schwartz (1995). Seismological evidence for magmatic and hydrothermal structure in Long Valley Caldera from local earthquake attenuation and velocity tomography. J. Geophys. Res., 100, 8311-8326, doi:10.1029/95JB00152.

Sato, H. and I. S. Sacks (1989). Anelasticity and thermal structure of the oceanic upper mantle: Temperature calibration with heat flow data. J. Geophys. Res., 94, 5705-5715, doi:10.1029/JB094iB05p05705.

Sato, H., I. S. Sacks and T. Murase (1989). The use of laboratory velocity data for estimating temperature and partial melt fraction in the low-velocity zone: Comparison with heat flow and electrical conductivity studies, J. Geophys. Res., 94, 5689-5704. doi:10.1029/JB094iB05p05689.

Saunders, M. A. (1995). Solution of sparse rectangular systems using LSQR and CRAIG. Bit Numer Math 35, 588-604, doi:10.1007/BF01739829.

Scarfì, L., E. Giampiccolo, C. Musumeci, D. Patanè and H. Zhang (2007). New insights on 3D crustal structure in southeastern Sicily (Italy) and tectonic implications from an adaptive mesh seismic tomography, Phys. Earth Planet. Int., 161, 74-85, doi:10.1016/j.pepi.2007.01.007.

Spakman, W. and H. Bijwaard (2001). Optimization of Cell Parameterizations for Tomographic Inverse Problems, Pure Appl. Geophys., 158, 1401-1423, doi:10.1007/PL00001227.

Stocker, R. L. and R. B. Gordon (1975). Velocity and internal friction in partial melts, J. Geophys. Res., 80, 4828-4836, doi:10.1029/JB080i035p04828.

Suryanata, P. B., S. Bijaksana, D. Dahrin, A. D.Nugraha et al. (2024). Subsurface structure of Bali Island inferred from magnetic and gravity modeling: new insights into volcanic activity and migration of volcanic centers, Int. J. Earth Sci. (Geol Rundsch), 113, 523-538, doi:10.1007/s00531-024-02398-7.

Syahbana, D. K., K. Kasbani, G. Suantika, O. Prambada et al. (2019). The 2017-19 activity at Mount Agung in Bali (Indonesia): Intense unrest, monitoring, crisis response, evacuation, and eruption, Sci. Rep., 9, 8848, doi:10.1038/s41598-019-45295-9.

Syracuse, E. M., C. H. Thurber and J. A. Power (2011). The Augustine magmatic system as revealed by seismic tomography and relocated earthquake hypocenters from 1994 through 2009, J. Geophys. Res., 116, B09306, doi:10.1029/2010JB008129.

Thurber, C. (1987). Seismic structure and tectonics of Kilauea Volcano (Hawaii), US Geological Survey Professional Paper 1350, in Volcanism in Hawaii, 38, 919-934.

Thurber, C. H. (1983). Earthquake locations and three-dimensional crustal structure in the Coyote Lake Area, central California, J. Geophys. Res., 88, 8226-8236, doi:10.1029/JB088iB10p08226.

Thurber, C. H., S. R. Atre and D. Eberhart-Phillips (1995). Three-dimensional Vp and Vp/Vs structure at Loma Prieta, California, from local earthquake tomography, Geophys. Res. Lett., 22, 3079-3082. doi:10.1029/95GL03077.

Um, J. and C. Thurber (1987). A fast algorithm for two-point seismic ray tracing, Bull. Seismol. Soc. Am., 77, 972-986. doi:10.1785/BSSA0770030972.

Vesnaver, A. L. (1996). Irregular grids in seismic tomography and minimum-time ray tracing, Geophys. J. Int., 126, 147-165, doi:10.1111/j.1365-246X.1996.tb05274.x.

Virtanen, P., R. Gommers, T. E. Oliphant, M. Haberland, T. Reddy et al. (2020). SciPy 1.0: fundamental algorithms for scientific computing in Python, Nat. Methods, 17, 261-272, doi:10.1038/s41592-019-0686-2.

Waldhauser, F. (2000). A Double-Difference Earthquake Location Algorithm: Method and Application to the Northern Hayward Fault, California, Bull. Seismol. Soc. Am., 90, 1353-1368, doi:10.1785/0120000006.

Westman, E., K. Luxbacher and S. Schafrik (2012). Passive seismic tomography for three-dimensional time-lapse imaging of mining-induced rock mass changes, The Leading Edge, 31, 338-345, doi:10.1190/1.3694902.

Widiyantoro, S. and R. Hilst (1997). Mantle structure beneath Indonesia inferred from high-resolution tomographic imaging, Geophys. J. Int., 130, 167-182,doi:10.1111/j.1365-246X.1997.tb00996.x.

Widiyantoro, S., M. Ramdhan, J.-P. Métaxian, P. R. Cummins et al. (2018). Seismic imaging and petrology explain highly explosive eruptions of Merapi Volcano, Indonesia, Sci, Rep., 8, doi:10.1038/s41598-018-31293-w.

Yang, H., X. Zhang and H. Zhang (2025). 3-D variational inference-based double-difference seismic tomography method and application to the SAFOD site, California, Geophys. J. Int., 241, 378-404, doi:10.1093/gji/ggaf040.

Yang, J., X. Shang, L. Liu, Y. Wang and X. Li (2026). Fast marching method-based bent-ray tracing for three-dimensional velocity imaging in mines, Rock Mechan. Bull., 5, 100262, doi:10.1016/j.rockmb.2025.100262.

Zhang, H. (200). Double-Difference Tomography: The Method and Its Application to the Hayward Fault, California, Bull. Seismol. Soc. of Am., 93, 1875-1889, doi:10.1785/0120020190.

Zhang, H. and C. Thurber (2005). Adaptive mesh seismic tomography based on tetrahedral and Voronoi diagrams: Application to Parkfield, California, J. Geophys. Res., 110, 2004JB003186, doi:10.1029/2004JB003186.

***CORRESPONDING AUTHOR: I Putu Raditya AMBARA PUTRA**
UPN Veteran Yogyakarta, Geophysical Engineering, Yogyakarta, Indonesia
e-mail: i.puturaditya@upnyk.ac.id

© 2026 the Author(s).
Open Access. This article is licensed under a Creative Commons Attribution 4.0 International License